

# 3D Part Segmentation via Geometric Aggregation of 2D Visual Features

Marco Garosi

University of Trento

marco.garosi@unitn.it

Massimiliano Mancini

University of Trento

massimiliano.mancini@unitn.it

Riccardo Tedoldi

University of Trento

riccardo.tedoldi@unitn.it

Nicu Sebe

University of Trento

sebe@disi.unitn.it

Davide Boscaini

Fondazione Bruno Kessler

dboscaini@fbk.eu

Fabio Poiesi

Fondazione Bruno Kessler

poiesi@fbk.eu

## Abstract

*Supervised 3D part segmentation models are tailored for a fixed set of objects and parts, limiting their transferability to open-set, real-world scenarios. Recent works have explored vision-language models (VLMs) as a promising alternative, using multi-view rendering and textual prompting to identify object parts. However, naively applying VLMs in this context introduces several drawbacks, such as the need for meticulous prompt engineering, and fails to leverage the 3D geometric structure of objects. To address these limitations, we propose COPS, a COMprehensive model for Parts Segmentation that blends the semantics extracted from visual concepts and 3D geometry to effectively identify object parts. COPS renders a point cloud from multiple viewpoints, extracts 2D features, projects them back to 3D, and uses a novel geometric-aware feature aggregation procedure to ensure spatial and semantic consistency. Finally, it clusters points into parts and labels them. We demonstrate that COPS is efficient, scalable, and achieves zero-shot state-of-the-art performance across five datasets, covering synthetic and real-world data, texture-less and coloured objects, as well as rigid and non-rigid shapes. The code is available at <https://3d-cops.github.io>.*

objects seen during training. In contrast, vision-language models (VLMs) can handle objects and parts that were not seen during training, making them more versatile in open-vocabulary settings [23, 24, 39].

In this context, methods such as PointCLIP [55, 59], PartSLIP [28, 57], ZeroPS [50], and SATR [1] leverage VLMs like CLIP [39] or GLIP [24] in a two-step procedure to tackle open-vocabulary settings. First, a point cloud is rendered into multiple views, which are then processed by the VLM’s visual encoder to extract visual features. Second, these visual features are projected back into 3D and compared with the text features derived from prompts describing object parts to produce the final segmentation. This approach suffers from two drawbacks: (i) it does not incorporate 3D geometric knowledge, and (ii) its performance depends on the quality of the input prompts (Fig. 1), as some parts can be challenging to describe in natural language. The latter issue can be partially addressed by crafting better textual prompts with the assistance of large language models such as ChatGPT [28, 57], or through prompt ensembles to reduce description ambiguity [39]. However, the inherent ambiguity of natural language remains a significant challenge, particularly when generalising to unseen objects and parts.

In this paper, we blend features from a 2D vision foundation model (VFM) with 3D geometric understanding to detect object parts. COPS follows a five-step procedure that involves: (i) rendering the object from multiple views that cover a large as possible portion of the object, (ii) extracting pixel-level features using DINOv2 [33] and upsampling its output, (iii) back-projecting these features onto the points, (iv) aggregating point-level features from multiple views using the geometric feature aggregation (GFA) module, and (v) segmenting object parts through unsupervised clustering of point-level features, followed by zero-shot classification. For tasks requiring only part decomposition without knowledge of part categories, the zero-shot classifier of COPS can be disabled to reduce computational costs and avoid inaccuracies caused by natural language ambiguities [26, 43].

## 1. Introduction

Recognising object parts has raised widespread attention in both industry and academia, with applications ranging from robotic manipulation [5, 14] to augmented reality [8]. Understanding and interacting with objects requires identifying their building components. For example, we open a bottle by detecting its cap, or hold a mug by its handle.

Currently, well-annotated 3D part segmentation datasets contain only a limited amount of samples in a restricted number of categories. This limits the transferability of models, as their knowledge is narrowed to the closed-set parts and

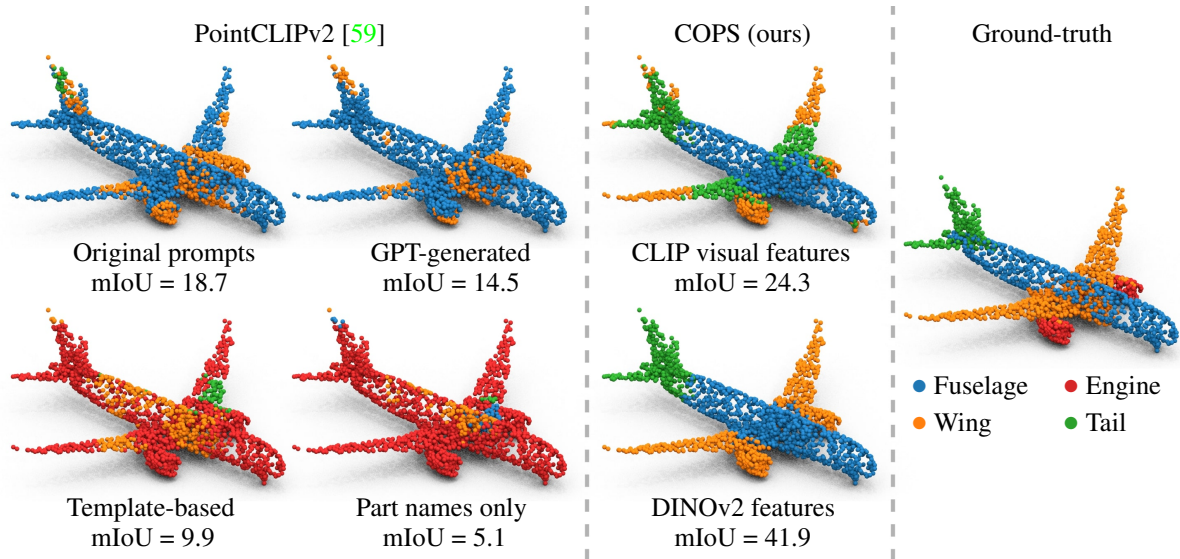


Figure 1. The quality of part descriptions significantly affects the segmentation performance of methods based on vision-language models. For example, the performance of PointCLIPv2 [59] (left) deteriorates rapidly when replacing the default textual prompt with a GPT-generated description, the template “This is a depth image of an airplane’s [part]”, or simply using part names. In contrast, our pipeline (center) achieves more accurate segmentations by disentangling part decomposition from part classification. The improvement is evident when using the same CLIP visual features as PointCLIPv2 (top) and becomes even more pronounced when using DINOv2 [33] features (bottom), the default choice of COPS. COPS generates more uniform segments with sharper boundaries, resulting in higher segmentation quality.

In summary, our contributions are:

- A novel training-free method for 3D part segmentation, which disentangles part segmentation from semantic labelling;
- A geometric feature aggregation module that fuses 3D structural information with semantic knowledge from VFMs;
- A thorough evaluation on five benchmarks, establishing a unified evaluation that future zero-shot part segmentation methods can use for comparison.

## 2. Related works

We identify two main approaches to 3D point cloud part segmentation: using networks specifically designed to handle 3D data natively and adapting 2D VLMs to the 3D task.

**3D networks for point cloud part segmentation.** A general approach to point cloud part segmentation [2, 30, 45, 52] is to leverage point-based methods [36, 37] that extract a semantic representation for each point. These works focus either on supervised or self-supervised methods [3, 4, 17, 25, 29, 46], and they produce feature representations that transfer well to the part segmentation task [36, 37, 40, 41]. Other works focus directly on part segmentation. They group points belonging to the same part by leveraging different strategies. The most common techniques are prototype-based, modelling and matching shape parts [18, 38, 53, 56], grouping [19, 27, 47, 49, 54], and directly training for point clustering. However, datasets with 3D annotated shapes are

scarce and costly to produce. Therefore, a thread of works explored the use of alternative supervision signals, such as bounding boxes [10], assembly manuals [48], and reference games [22]. Similarly, other works introduced unsupervised objectives, such as learning hierarchies [32], co-segmentation [9, 51, 58], abstraction [12, 15, 34, 35, 42]. In addition to data scarcity, some methods have to face costly training procedures, which results in limited transfer learning capabilities and robustness to domain gaps and unseen objects. With COPS, we overcome all these limitations by offering a training-free, efficient, and versatile solution.

**Adapting 2D VLMs to 3D tasks.** Several VLM-based methods aim to segment 3D objects into parts with a three-stage approach: (i) generating multiple 2D views of the object, (ii) extracting the features from each view, (iii) projecting 2D features onto 3D points. However, aligning visual and text modalities requires carefully tuned prompts, which must be effectively matched to visual prompts. For example, PointCLIP [55] and PointCLIPv2 [59] utilise CLIP [39] for segmenting objects into parts. DILF [31] extended PointCLIPv2 [59] by incorporating a fully differentiable renderer to learn optimal camera poses for specific datasets. In contrast to these methods, the segmentation quality of COPS does not depend on prompts, as we utilise them only to label already-segmented parts. PartSLIP [28] is a bounding-box-based framework for part segmentation that uses GLIP [24]. Its successor [57] introduces SAM [21] and an expectation-maximisation algorithm to improve predictions. Subsequent works [1, 44, 50] build upon PartSLIP to enhance the part

segmentation quality. These detection-based methods rely on bounding boxes to back-project categorical labels to the points, while COPS projects features to points.

### 3. Our approach

COPS consists of five-stages, as depicted in Fig. 2. First, the point cloud is rendered into multiple 2D images. Next, we extract features with a 2D vision foundation model and subsequently project them back onto 3D points, obtaining point-level semantic features. These steps eliminate the need for models specifically crafted and trained for 3D tasks, thus avoiding the need for annotated data. We introduce a geometric feature aggregation module, or GFA, that combines visual features from geometrically neighbouring and semantically similar points to produce novel features that incorporate both the point’s semantic (*i.e.*, what part it belongs to) and geometry (*i.e.*, how it relates to other points). Lastly, we attain open-vocabulary by integrating predictions from a VLM, which assigns a semantic label to each part. Differently from our competitors [55, 59], we do not require meticulously crafted prompts, as the VLM is leveraged for part-level labelling, rather than point-level labelling.

#### 3.1. Problem formulation

Given a point cloud of an object and a list of parts, our goal is to segment the point cloud into its constituent parts and label them according to the given list. Formally, let  $\mathcal{X} = (\mathcal{X}^p | \mathcal{X}^c) \in \mathbb{R}^{N \times 6}$  denote a point cloud with  $N$  vertices, where  $\mathcal{X}^p \in \mathbb{R}^{N \times 3}$  encodes positional information as XYZ coordinates,  $\mathcal{X}^c \in \mathbb{R}^{N \times 3}$  encodes photometric information (when available) as RGB colours, and  $|$  denotes concatenation along the last dimension. We assume  $\mathcal{X}$  to have  $P$  parts, *i.e.*,  $\mathcal{X} = \bigcup_{p=1}^P \mathcal{X}_p$ , and we denote the set of point-level part labels as  $\mathcal{Y} \in \{1, \dots, P\}^N$ . COPS consists of two main components: a feature extractor  $\Phi$ , and a segmenter  $\Psi$ .  $\Phi: \mathcal{X} \mapsto \mathcal{F} \in \mathbb{R}^{N \times d}$  is a function that maps input points into  $d$ -dimensional features. Next,  $\Psi: \mathcal{F} \mapsto \tilde{\mathcal{Y}} \in \{1, \dots, P\}^N$  converts point-wise features into categorical labels that identify the input’s parts. Following [55, 59], we measure the segmentation quality as the mean intersection-over-union (mIoU) between our prediction  $\tilde{\mathcal{Y}}$  and the ground truth  $\mathcal{Y}$ .

#### 3.2. Feature extraction

The feature extractor  $\Phi$  consists of two parts: a feature encoder  $\Phi_{\mathcal{E}}$  and a geometric feature aggregation module  $\Phi_{\text{GFA}}$ . Thus,  $\Phi = \Phi_{\text{GFA}} \circ \Phi_{\mathcal{E}}$ . This section discusses  $\Phi_{\mathcal{E}}$ , while the following one presents  $\Phi_{\text{GFA}}$ .  $\Phi_{\mathcal{E}}$  comprises three parts: (i) point cloud rasterization, which turns the input into a collection of 2D images; (ii) 2D feature extraction; and (iii) feature back-projection onto 3D points.

**Point cloud rasterization.** One of the goals of COPS is to avoid training. Therefore, we employ a frozen pre-trained

2D vision model, DINOv2 [33] in our case, to extract features. However, these models are designed for image inputs and cannot operate directly on 3D data. To overcome this limitation, we rasterize the input point cloud into a collection of images, capturing the input from various angles. We rasterize  $\mathcal{X}$  from  $R$  pre-defined camera viewpoints sampled from a unit sphere around the object to obtain the set of images  $\{\mathbf{I}_r\}_{r=1}^R$ . If  $\mathcal{X}$  contains only coordinate information,  $\mathbf{I}_r \in [0, 1]^{H \times W}$  are greyscale (non-metric) depth maps. If  $\mathcal{X}$  also contains photometric information associated with each point,  $\mathbf{I}_r \in [0, 1]^{H \times W \times 3}$  are RGB images.

Unlike [55, 59], during rendering we do not subsample the point cloud. As a consequence, our model produces higher-quality renders that look more photorealistic and close the gap with the VFM’s training data. Additionally, we have chosen to retain the background of the point cloud when it is provided (*e.g.*, in ScanObjectNN [45]). This increases the task’s difficulty, as it can add noise, either surrounding the point cloud or introducing other objects in the scene.

**2D feature extraction.** We can now extract features from the images obtained in the previous step. Let us denote with  $\Gamma_{\Theta}$  the VFM with parameters  $\Theta$ . We implement  $\Gamma_{\Theta}$  with DINOv2 [33], keeping its parameters  $\Theta$  frozen. To perform part segmentation, we require dense features, but most VFMs, including DINOv2, are ViT-based [13], thus providing only patch-level features. Therefore, we obtain pixel-level features for each image  $\mathbf{I}_r$  by interpolating the patch-level ones with a bicubic interpolator  $\Pi$ , resulting in  $\Pi \circ \Gamma_{\Theta}(\mathbf{I}_r) = \mathbf{H}_r \in \mathbb{R}^{H \times W \times d}$ , where  $H \times W$  is the resolution of  $\mathbf{I}_r$  and  $d$  is the feature size.

**Feature back-projection.** As a last step, we need to bring the 2D features to the 3D points. We achieve this via back-projection, which exploits the correspondence  $\zeta: \mathbf{I}_r \rightarrow \mathcal{X}$  between the pixels  $\mathbf{p}_{ij}$  of a rendered 2D image and the 3D points  $\mathbf{x}_k$  of  $\mathcal{X}$ . The  $\zeta$  is a byproduct of the rasterization procedure, requiring no additional computation. Let  $\mathbf{x}_i \in \mathcal{X}$  be the  $i^{\text{th}}$  point of the point cloud and  $\mathcal{Z}_i \in \zeta$  the set of pixel-to-point mappings for the  $i^{\text{th}}$  point,  $\mathbf{z}_{ir}$  being the mapping for the  $i^{\text{th}}$  point in the rendered image  $\mathbf{I}_r$ . The feature vector  $\mathbf{f}_i \in \mathbb{R}^d$  for  $\mathbf{x}_i$  is computed as:

$$\mathbf{f}_i = \frac{1}{|\mathcal{Z}_i|} \sum_{\mathbf{z}_{ir} \in \mathcal{Z}_i} \mathbf{H}_r[\mathbf{z}_{ir}], \quad (1)$$

which gets the pixel coordinates of  $\mathbf{x}_j$  in each view and averages the features of such pixels. This back-projection mechanism provides a linear combination of features, therefore being scalable and computationally cheaper than other approaches that filter foreground content (*e.g.*, [1, 20, 28, 57]). Lastly, some points might be invisible in all views. According to geometric consistency, *i.e.*, points that are close in space likely belong to the same part, COPS estimates features for hidden points by averaging those of their  $L = 20$  nearest neighbours in 3D space.



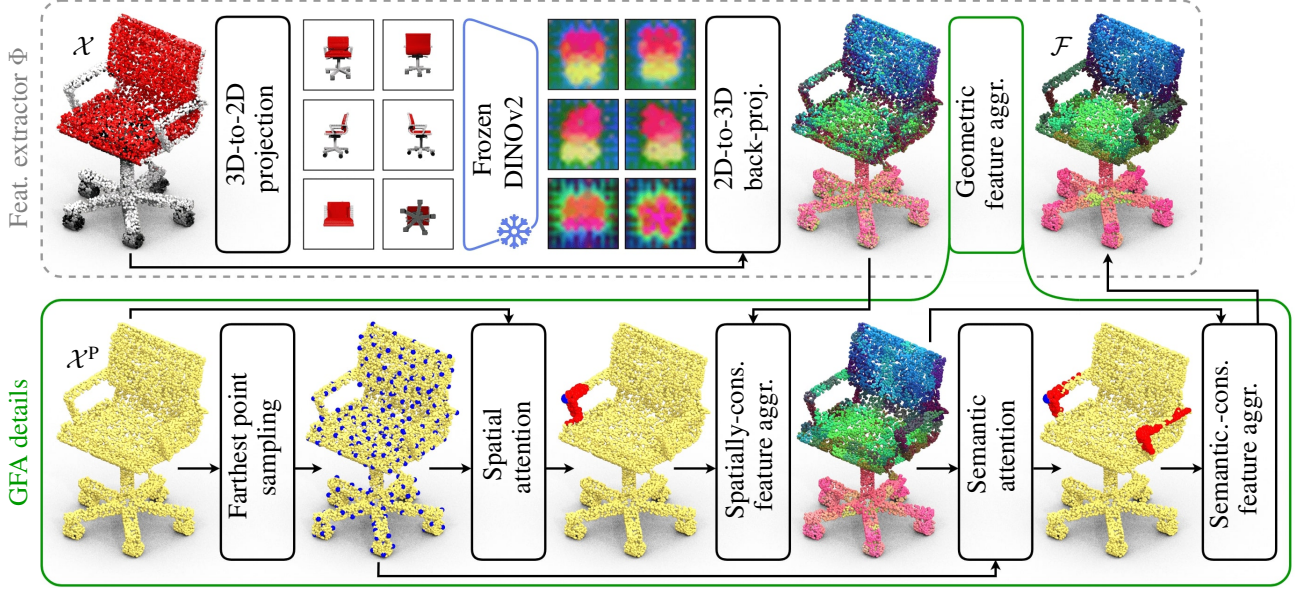


Figure 2. Overview of COPS’s feature extractor.  $\Phi$  (top) extracts point-level features by (i) rendering multiple views of the object, (ii) processing them with DINOv2, (iii) lifting them in 3D. The Geometric Feature Aggregation module (GFA, bottom) further refines these features by extracting super points (blue points in the second row) and their neighbouring points (red points in the second row) to obtain spatially consistent centroids. These centroids are used to perform spatial- and semantic-consistent feature aggregation, ensuring that the features are both locally consistent and similar across large distances when describing the same part (e.g., the armrest).

### 3.3. Geometric feature aggregation (GFA)

The features extracted with  $\mathcal{F} = \Phi_{\mathcal{E}}$  are derived from 2D views, thus lacking spatial and semantic consistency that are keys to creating coherent and robust 3D representations. In the following, we describe how we refine  $\mathcal{F}$  with two consecutive steps, spatially- and semantically-consistent GFA. In Sec. 4.4, we refer to Eq. (1) as “baseline”.

**Spatially-consistent GFA** performs geometric reasoning at the coordinate level, i.e.,  $\mathcal{X}^P$ . It follows two main principles: (i) model point cloud regions via centroids, (ii) propagate features from super points to the original ones. We extract a set of  $M$  centroids  $\mathcal{C} = \{\mathbf{x}_m \in \mathcal{X}^P\}_{m=1}^M$  by farthest point sampling (FPS) on  $\mathcal{X}^P$ . For each centroid  $\mathbf{c} \in \mathcal{C}$ , we collect the features associated with its  $K$  nearest neighbours  $\mathcal{X}_c = \{\mathbf{x}_j\}_{j=1}^K \in \mathcal{X}^P$ , and update the centroid’s features by computing their average:

$$\mathbf{f}_c = \frac{1}{K} \sum_{\mathbf{x}_i \in \mathcal{X}_c} \mathbf{f}_i. \quad (2)$$

Once the centroid features are updated, we update the features of the original points, i.e.,  $\mathcal{X} \setminus \mathcal{C}$ , via interpolation:

$$\mathbf{f}_i^{\text{spatial}} = \frac{1}{K'} \sum_{\mathbf{c} \in \mathcal{C}_{K'}} \mathbf{f}_c, \quad (3)$$

where  $\mathcal{C}_{K'}$  are the  $K'$  closest centroids  $\mathbf{c}$  to point  $i$ . Therefore, the feature vector of each point is influenced by the closest centroids, obtaining spatially consistent features (Eq. (3)) that encode the geometrical relationships of points.

**Semantically-consistent GFA** refines the spatially consistent features by performing geometric reasoning at the feature level, i.e.,  $\mathcal{F}$ . Similarly to the spatially-consistent counterpart, we still extract  $\mathcal{C}$  via FPS, but the  $K$  nearest neighbours are computed in the feature space rather than in the coordinate space, i.e.,  $\mathcal{F}_c = \{\mathbf{f}_j\}_{j=1}^K \in \mathcal{F}$ . The features of the centroid  $c$  are updated as:

$$\mathbf{f}_c^{\text{semantic}} = \frac{1}{K} \sum_{\mathbf{f}_i \in \mathcal{F}_c} \mathbf{f}_i^{\text{spatial}}, \quad (4)$$

where the closest points are retrieved directly in the feature space. The final point-level features are obtained as:

$$\hat{\mathbf{f}}_i = \frac{1}{K'} \sum_{\mathbf{f}_c \in \mathcal{C}_{K'}} \mathbf{f}_c^{\text{semantic}}, \quad (5)$$

where  $\mathcal{C}_{K'}$  are the  $K'$  closest centroids  $\mathbf{c}$  to point  $i$ . We term this aggregation mechanism semantically-consistent because neighbouring features correspond to points that have a similar semantic but that can be distant in the coordinate space (e.g., the wheels of an office chair). This module operates under the assumption that the VFM maps semantically similar points to close regions of the latent space.

### 3.4. Zero-shot part segmentation head

This section discusses  $\Psi: \mathcal{F} \mapsto \hat{\mathcal{Y}} \in \{1, \dots, P\}^N$ , which requires no specific training for our task.  $\Psi$  enables zero-shot 3D part segmentation by performing: (i) *shape-level clustering*, (ii) *language-driven semantic anchors extraction*, and (iii) *label alignment* to classify parts.



**Shape-level clustering.** We cluster the point-level features  $\mathcal{F}$  to obtain candidate parts. Given a target of  $P$  parts, we apply K-means to split the point cloud into  $P$  regions  $\{\mathcal{X}_1, \dots, \mathcal{X}_P\}$ . Clustering takes advantage of the spatially and semantically consistent features extracted via Eq. (5).

**Semantic anchors extraction.** At this stage, the obtained parts lack a direct link to natural language, as there is no mapping from cluster index to categorical label. We exploit the capabilities of VLMs to provide such a mapping, which is required to compare fairly with our competitors. We note that this step is not strictly necessary, *e.g.*, for applications that do not require this mapping but simply require parts.

We employ a VLM, CLIP in our case following [55, 59], to encode both the rendered views of the object and textual descriptions of the target parts. These can be only the part name, manually annotated descriptions, or LLM-based ones: we analyse all these options in our ablation study. Next, we compute the cosine similarity between the 2D visual features and the textual embeddings. We back-project these scores to 3D exploiting the same function  $\zeta$  defined in Eq. (1), and we classify the point with the label with the highest similarity. Lastly, we group points by label, obtaining  $P$  segmentation masks, denoted as  $\{\hat{\mathcal{Y}}_1, \dots, \hat{\mathcal{Y}}_P\}$ .

**Final segmentation.** The last step is to assign semantic labels to the clusters by mapping each cluster  $\mathcal{X}_i$  to a segmentation mask  $\hat{\mathcal{Y}}_j$ . To ensure each mask is assigned to only one cluster, we use the Hungarian algorithm to measure the overlap between the set of points for each pair  $(\mathcal{X}_i, \hat{\mathcal{Y}}_j)$ .

## 4. Experimental results

### 4.1. Benchmark details

**Datasets.** We evaluate COPS on five part segmentation datasets, including the synthetic datasets ShapeNetPart [52], PartNet [30], and PartNetE [28], and the real-world datasets ScanObjectNN [45] and FAUST [2]. ShapeNetPart [52] contains 2,874 point clouds, spread across 16 categories. It provides no photometric information. Next, PartNet [30] is a larger and more diverse dataset with 24 categories comprising 26,671 objects, of which 5,169 are in the test set. Points provide colour information. Following PartNetE [28] is a subset of PartNet containing 1,906 test set point clouds with colour. Fourth, ScanObjectNN [45] provides 15 categories with a total of 2,902 real-world textured point clouds (580 in the test set). Point clouds are provided both without (OBJ-ONLY) and with (OBJ-BG) background, which can provide context but also introduce noise. Finally, FAUST [2] contains 300 untextured real human scans of 10 different subjects in various poses. We utilise the coarse-grained part annotations proposed in SATR [1].

**Metrics.** We measure performance as the mean Intersection over Union (mIoU) between our prediction and the ground truth, reporting both: (i) class-average, which averages the mIoU of point clouds in the same category, and then averages

class IoUs; and (ii) instance-average IoU, which averages the mIoU of all objects, regardless of their class. Following our competitors in Tab. 3, we use the average IoU (aIoU) [50]. We also report results when measuring segmentation quality without assigning semantic labels to parts, indicating it with “↑”. This shows the upper bound COPS can achieve when a *perfect* labeller is employed. This setting may be useful when the downstream task does not require semantic labels, but only which parts compose the object.

**Baselines.** We compare COPS to other methods that leverage VLMs. When there are no direct competitors, we use PointCLIPv2 as our baseline. Because there are different implementations of evaluation metrics, we meticulously checked other methods’ source code to ensure comparable results.

**Implementation details.** We use DINOv2 base [33] as VFM and CLIP ViT-B/16 [39] for semantic labelling. We render 48 RGBD images per point cloud, with a point size of 0.01 or 0.04 depending on the density of the dataset.

### 4.2. Quantitative results

Tab. 1 shows results on ShapeNetPart. COPS outperforms PointCLIPv2, the previous state-of-the-art model, by a significant margin of +10.7% in instance average mIoU and +6.3% in class average. We show results on all 16 categories, observing a consistent increase over 13 categories, scoring +17.4% on Chair, +15.7% on Cap, and +18.0% on Airplane. Tab. 2 reports scores on the PartNet dataset. Since no other model is competing in our setting, *i.e.*, zero-shot part segmentation, on this dataset, we provide a baseline by running PointCLIPv2. Results are obtained by using GPT-generated prompts, similar to [59] but excluding the post-search optimisation phase. We show detailed results for 12 out of 24 categories. COPS outperforms the baseline on 21 categories, achieving a considerable margin of +6.1% on Door, +7.4% on Display, and +7.5% on Earphone. Overall, our model surpasses PointCLIPv2 by +4.8% in instance-average and +3.8% in class-average. We also compare with PartNetE [28] in Tab. 3, reporting 12 out of 45 categories. COPS surpasses both PartSLIP [28] and ZeroPS [50] by +0.2%, with improvements of up to +24.2% on Box and +24.4% on Safe. Tab. 4 presents a detailed comparison on the challenging OBJ-BG setting of the real-world ScanObjectNN dataset. COPS outperforms across all categories, with gains as high as +15.7% on Cabinet. The model effectively reduces the labeller’s noise, achieving improvements of +9.6% in instance-average mIoU and +8.7% in class-average mIoU. Tab. 5 shows performance on FAUST [2], with detailed results on the four coarse-grained parts annotated by SATR [1]. COPS surpasses PointCLIPv2 by +16.8%. We do not compare with 3DH [11] and SATR [1], as they operate with triangular meshes that capture finer details compared to point clouds, making a direct comparison unfair.

Method	mIoU <sub>I</sub>	mIoU <sub>C</sub>	Airplane	Bag	Cap	Car	Chair	Earph.	Guitar	Knife	Lamp	Laptop	Motor.	Mug	Pistol	Rocket	Skate	Table
Instances	2874		341	14	11	158	704	14	159	80	286	83	51	38	44	12	31	848
1 3DH [11]	9.6	5.7	5.8	2.1	2.9	2.9	15.5	9.6	0.9	1.6	13.2	1.8	5.6	0.7	1.4	10.4	6.4	10.8
2 SATR [1]	32.8	31.9	38.5	44.6	24.0	19.6	33.2	16.9	40.2	45.9	30.2	37.8	15.7	52.3	20.9	28.4	30.8	31.4
3 PointCLIP [55]	24.8	29.8	22.0	44.8	13.4	-	18.7	28.3	22.7	24.8	-	22.9	-	48.6	-	22.7	42.7	45.5
4 PointCLIPv2 [59]	51.8	51.0	33.4	60.4	52.9	27.2	51.6	56.5	<b>71.5</b>	<b>76.7</b>	44.7	61.5	<b>31.5</b>	48.0	46.1	49.6	43.9	61.1
5 COPS	<b>62.5</b>	<b>57.3</b>	<b>51.4</b>	<b>67.8</b>	<b>68.6</b>	<b>30.1</b>	<b>69.0</b>	<b>60.9</b>	63.5	76.3	<b>48.2</b>	<b>70.0</b>	22.8	<b>53.7</b>	<b>51.1</b>	<b>50.5</b>	<b>59.1</b>	<b>73.6</b>
6 COPS ↑	72.1	65.0	62.3	72.2	78.7	38.7	80.8	72.3	62.6	78.0	77.2	73.4	26.5	65.3	52.5	53.6	66.4	78.8
7 Improvement	+10.7	+6.3	+18.0	+7.4	+15.7	+2.9	+17.4	+4.4	-8.0	-0.4	+3.5	+8.5	-8.7	+5.7	+5.0	+0.9	+15.2	+12.5

Table 1. Zero-shot part segmentation results on ShapeNetPart [52]. In this Table and Tab. 2, Tab. 3, and Tab. 4 we report results in terms of mean IoU across instances (mIoU<sub>I</sub>) and categories (mIoU<sub>C</sub>). Some categories for PointCLIP are missing since the authors of PointCLIPv2, who adapted it to part segmentation, do not report them. Row 7 shows our improvement over row 4, the best-performing competitor.

Method	mIoU <sub>I</sub>	mIoU <sub>C</sub>	Bottle	Bowl	Clock	Displ.	Door	Earph.	Faucet	Knife	Lamp	Micro.	Table	Vase
Instances	5169		1668	39	98	191	51	53	132	77	419	39	1668	233
1 PointCLIPv2 [59]	34.0	35.1	39.0	25.6	17.8	47.3	43.7	24.3	21.1	34.1	54.3	<b>57.5</b>	46.0	30.8
2 COPS	<b>38.8</b>	<b>38.9</b>	<b>44.6</b>	<b>29.2</b>	<b>22.0</b>	<b>54.7</b>	<b>49.8</b>	<b>31.8</b>	<b>22.6</b>	<b>35.3</b>	<b>55.0</b>	55.1	<b>46.3</b>	<b>36.8</b>
3 COPS ↑	85.6	79.1	79.8	89.6	91.4	85.3	81.6	90.6	82.7	93.2	95.9	80.6	94.5	92.1
4 Improvement	+4.8	+3.8	+5.6	+3.6	+4.2	+7.4	+6.1	+7.5	+1.5	+1.2	+0.7	-2.4	+0.3	+6.0

Table 2. Zero-shot part segmentation results on PartNet [30]. We show details about 12 out of the 24 total categories.

Method	aIoU <sub>I</sub>	aIoU <sub>C</sub>	Clock	Door	Knife	Table	Box	Lighter	Oven	Pen	Safe	Stapler	Suitcase	Toaster
Instances	1906		23	28	36	93	20	20	22	40	22	15	16	17
1 PartSLIP [57]	-	36.4	17.8	27.9	18.3	46.9	38.8	53.2	22.8	44.6	17.4	27.3	65.8	19.7
2 ZeroPS [50]	-	56.0	33.8	37.8	68.7	53.3	63.1	<b>64.4</b>	37.0	71.7	26.2	<b>80.7</b>	62.2	<b>62.7</b>
3 COPS	<b>55.8</b>	<b>56.2</b>	<b>41.8</b>	<b>46.0</b>	<b>69.4</b>	<b>63.5</b>	<b>87.3</b>	60.0	<b>53.4</b>	<b>73.9</b>	<b>50.6</b>	58.1	<b>65.2</b>	34.5
4 Improvement	-	+0.2	+8.0	+8.2	+0.7	+10.2	+24.2	-4.4	+16.4	+2.2	+24.4	-22.6	+3.0	-27.7

Table 3. Zero-shot part segmentation results on PartNetE [28]. We report 12 out of 45 categories. Following our competitors, we measure performance with the Average IoU (aIoU). Row 4 shows our improvement over row 2, the best-performing competitor.

Method	mIoU <sub>I</sub>	mIoU <sub>C</sub>	Bag	Bed	Bin	Box	Cabin.	Chair	Desk	Displ.	Door	Pillow	Shelf	Sink	Sofa	Table	Toilet
Instances	583		14	45	20	68	109	34	27	41	57	44	26	40	20	17	21
1 PointCLIPv2 [59]	10.6	11.6	12.7	5.1	3.5	8.3	9.5	9.1	21.4	19.6	5.4	11.8	17.6	30.0	8.4	6.5	5.0
2 COPS	<b>20.2</b>	<b>20.3</b>	<b>19.1</b>	<b>9.3</b>	<b>10.1</b>	<b>14.0</b>	<b>25.2</b>	<b>17.5</b>	<b>31.4</b>	<b>24.8</b>	<b>14.1</b>	<b>23.3</b>	<b>31.7</b>	<b>39.3</b>	<b>13.6</b>	<b>20.7</b>	<b>10.8</b>
3 COPS ↑	63.0	62.2	69.9	74.7	81.8	75.7	65.3	46.9	52.3	54.1	65.2	59.6	50.0	59.2	57.4	51.5	69.5
4 Improvement	+9.6	+8.7	+6.4	+4.2	+6.6	+5.7	+15.7	+8.4	+10.0	+5.2	+8.7	+11.5	+14.1	+9.3	+5.2	+14.2	+5.8

Table 4. Zero-shot part segmentation results on the OBJ-BG variant of ScanObjectNN [45]. All 15 categories are reported.

Input	Method	mIoU	Arm	Head	Leg	Torso
mesh	1 3DH [11]	16.5	28.6	14.2	14.9	8.2
	2 SATR [1]	82.5	85.9	90.6	85.8	67.6
	3 PointCLIPv2 [59]	13.6	14.0	15.8	24.1	0.3
	4 COPS	<b>30.4</b>	<b>29.8</b>	<b>33.4</b>	<b>48.2</b>	<b>10.2</b>
	5 COPS ↑	64.7	72.4	79.7	62.2	42.3
	6 Improvement	+16.8	+15.8	+17.6	+24.1	+9.9

Table 5. Zero-shot part segmentation results on the coarse-grained variant of FAUST [1] in terms of mean IoU (mIoU). We show details about all the four parts, and directly compare with the only competitor that uses point clouds data.

### 4.3. Qualitative results

Fig. 3 shows a qualitative comparison between our method and PointCLIPv2 on ShapeNetPart [52] with seven shapes that cover various categories, *e.g.*, Airplane and Skateboard. Fig. 4 shows the comparison on five shapes from ScanObjectNN [45] OBJ-BG (the same as Tab. 4). In both Figures, we observe the superior quality of segmentations produced by COPS thanks to (i) the decoupling of part segmentation and semantic label assignment, and (ii) the GFA module that makes the VFM’s features geometric-aware by introducing structural knowledge.

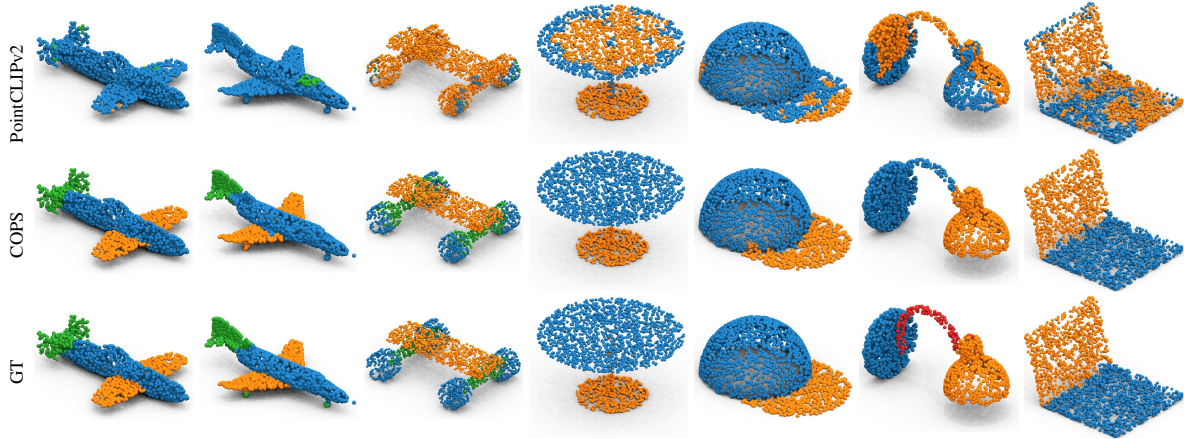


Figure 3. Qualitative results on ShapeNetPart [52]. Top to bottom: PointCLIPv2 [59], COPS, ground-truth. These results show that PointCLIPv2 often struggles in describing and segmenting some parts, such as the wheels of the skateboard or the wings of the plane. COPS instead produces a better segmentation, with more uniform part segments and sharper part boundaries.



Figure 4. Qualitative results on ScanObjectNN [45]. Top to bottom: input point cloud with color information; PointCLIPv2’s prediction; COPS’s prediction; ground-truth segmentation. COPS outputs better and sharper segmentations than PointCLIPv2.

#### 4.4. Ablation study

In Fig. 5, we conduct an ablation study of COPS on ShapeNetPart [52]. We analyse: (a) the influence of prompting techniques and (b) rendered views on semantic label assignment, (c) the effects of the type of VFM and (d) the GFA module design on feature extraction.

**Prompt type.** Fig. 5(a) compares COPS with PointCLIPv2 with three distinct prompting methodologies: (i) the prompts

of PointCLIPv2 [59] (‘Orig.’), generated with GPT, (ii) template prompts containing part names (‘Temp.’) and (iii) utilising part names alone (‘Parts’). COPS always outperforms PointCLIPv2, with a margin of up to +13.1%. For ‘Orig.’, PointCLIPv2 searches for the best-performing prompts for each part. Following this, our experiments suggest that these specifically chosen prompts lead to a performance boost compared to the other strategies.



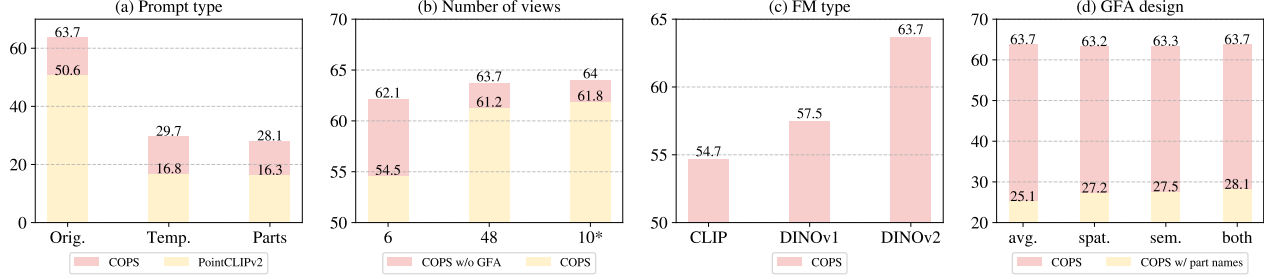


Figure 5. Ablation on ShapeNetPart [7]. From left to right: (a) Different prompt types, comparing PointCLIPv2 [59] and COPS. (b) Varying the number of views during rendering, with and without our GFA module. (c) Changing the foundation model. (d) Ablating the GFA module.

**Number of rendered views.** Fig. 5(b) assesses the impact of the number of rendered views. We test three different settings: (i) 6 orthogonal views, following SimpleView [16]; (ii) 48 views, sampled around the object to ensure a good covering of all viewpoints; (iii) 10 views, following PointCLIPv2 [59]. For each setting, we show the result of COPS both with and without the GFA module, and we utilise the same parts’ descriptions provided by PointCLIPv2. We observe that increasing the number of views from 6 to 10 leads to a boost in performance of +7.3% (+2.3% with GFA), while further increasing it from 10 to 48 has a negative effect, with -0.6% (-0.7% with GFA). We suggest that this may be due to a noise increment in the features extracted from *unusual* views (e.g., potentially out of distribution, or not capturing the object properly) when using the 48-view setting. We also show the effectiveness of our full GFA module, which always increases performance and reduces the gap between different numbers of views.

**VFM type.** Fig. 5(c) investigates the contribution of the VFM  $\Gamma_{\Theta}$  used in  $\Phi_{\mathcal{E}}$ . Specifically, we compare the CLIP [39] visual encoder and DINOv1 [6] to our default choice, DINOv2 [33], using the same ViT-B [13] backbone for all models to ensure a fair comparison. We utilise the same prompts provided by PointCLIPv2 (‘Orig.’ from (a)) and the same 48 rendered views from (b). When integrating CLIP within our pipeline, we observe an improvement of +4.1% over PointCLIPv2, as evidenced by comparing against the first bin of (a). This indicates the effectiveness of our two-step approach, which first decomposes a shape into parts before classifying them. Next, DINOv1 further boosts performance by +2.8%, suggesting that its self-supervised features are better suited for our task than CLIP’s text-aligned visual features. DINOv2 achieves the best results, with significant improvements of +6.2% (w.r.t. DINOv1) and +9% (w.r.t. CLIP).

**GFA design.** Fig. 5(d) analyses the contribution of our geometric feature aggregation (GFA) module in four distinct settings: (i) ‘avg.’, which simply performs average pooling; (ii) ‘spat.’, which performs spatially-consistent aggregation only; (iii) ‘sem.’, which performs semantically-consistent aggregation only; (iv) ‘both’, which is our final GFA de-

sign for COPS, leveraging both spatially- and semantically-consistent aggregation. For all settings, we measure performance both when using simple prompts (‘Parts’ in (a)), and when using PointCLIPv2’s descriptions (‘Orig.’ in (a)). In both cases, we observe an increasing boost in performance due to GFA. Spatially-consistent aggregation introduces 3D structural knowledge: for instance, the points in an armrest *exchange* information, thus increasing their feature similarity. Similarly, semantically-consistent aggregation makes features semantic-aware: for example, the two armrests of a chair will share information, getting closer to each other in feature space. Our final GFA design performs (ii) followed by (iii), improving performance of up to +3%.

## 5. Conclusion

In this work, we presented COPS, a zero-shot model for part segmentation that splits the task into part decomposition and semantic labelling. We introduced a geometric feature aggregation (GFA) module that fuses the features extracted by the vision foundation model on rendered views with geometric knowledge of the point cloud itself. We conducted extensive evaluations on part segmentation datasets showing COPS’s strong performance in all these settings.

**Limitations.** Thanks to the decoupling of part decomposition and semantic labelling, COPS can segment parts regardless of natural language, as we show in “↑” experiments in the tables. However, as natural language is still needed when part semantic labels are required for the downstream task, low-quality prompts negatively affect part classification.

**Future work.** COPS may be extended to cover new tasks, such as indoor scene segmentation, where LiDAR or RGB-D acquisition sensors provide point clouds and images, thereby eliminating the need for rendering. Architecture-wise, a learning-based module may be introduced to dynamically weight the features across multiple views.

## Acknowledgements

This work was supported by the European Union’s Horizon Europe research and innovation programme under grant agreement No. 101058589 (AI-PRISM).

## References

- [1] Ahmed Abdelreheem, Ivan Skorokhodov, Maks Ovsjanikov, and Peter Wonka. SATR: Zero-Shot Semantic Segmentation of 3D Shapes. In *ICCV*, 2023. 1, 2, 3, 5, 6
- [2] Federica Bogo, Javier Romero, Matthew Loper, and Michael J. Black. FAUST: Dataset and evaluation for 3D mesh registration. In *CVPR*, 2014. 2, 5
- [3] D. Boscaini, J. Masci, S. Melzi, M. M. Bronstein, U. Castellani, and P. Vanderghenst. Learning class-specific descriptors for deformable shapes using localized spectral convolutional networks. *Computer Graphics Forum*, 34(5), 2015. 2
- [4] Davide Boscaini and Fabio Poiesi. Patchmixer: Rethinking network design to boost generalization for 3d point cloud understanding. *Image and Vision Computing*, 137:104768, 2023. 2
- [5] Anthony Brohan, Noah Brown, Justice Carbajal, Yevgen Chebotar, Xi Chen, Krzysztof Choromanski, Tianli Ding, Danny Driess, Avinava Dubey, Chelsea Finn, Pete Florence, Chuyuan Fu, Montse Gonzalez Arenas, Keerthana Gopalakrishnan, Kehang Han, Karol Hausman, Alexander Herzog, Jasmine Hsu, Brian Ichter, Alex Irpan, Nikhil Joshi, Ryan Julian, Dmitry Kalashnikov, Yuheng Kuang, Isabel Leal, Lisa Lee, Tsang-Wei Edward Lee, Sergey Levine, Yao Lu, Henryk Michalewski, Igor Mordatch, Karl Pertsch, Kanishka Rao, Krista Reymann, Michael Ryoo, Grecia Salazar, Pannag Sanketi, Pierre Sermanet, Jaspiar Singh, Anikait Singh, Radu Soricut, Huong Tran, Vincent Vanhoucke, Quan Vuong, Ayzaan Wahid, Stefan Welker, Paul Wohlhart, Jialin Wu, Fei Xia, Ted Xiao, Peng Xu, Sichun Xu, Tianhe Yu, and Brianna Zitkovich. Rt-2: Vision-language-action models transfer web knowledge to robotic control, 2023. 1
- [6] Mathilde Caron, Hugo Touvron, Ishan Misra, Hervé Jégou, Julien Mairal, Piotr Bojanowski, and Armand Joulin. Emerging properties in self-supervised vision transformers. In *ICCV*, 2021. 8
- [7] Angel X. Chang, Thomas Funkhouser, Leonidas Guibas, Pat Hanrahan, Qixing Huang, Zimo Li, Silvio Savarese, Manolis Savva, Shuran Song, Hao Su, Jianxiong Xiao, Li Yi, and Fisher Yu. Shapenet: An information-rich 3d model repository, 2015. 8
- [8] Boyuan Chen, Zhuo Xu, Sean Kirmani, Brian Ichter, Danny Driess, Pete Florence, Dorsa Sadigh, Leonidas Guibas, and Fei Xia. Spatialvlm: Endowing vision-language models with spatial reasoning capabilities, 2024. 1
- [9] Zhiqin Chen, Kangxue Yin, Matthew Fisher, Siddhartha Chaudhuri, and Hao Zhang. Bae-net: Branched autoencoder for shape co-segmentation. In *ICCV*, 2019. 2
- [10] Julian Chibane, Francis Engelmann, Tuan Anh Tran, and Gerard Pons-Moll. Box2mask: Weakly supervised 3d semantic instance segmentation using bounding boxes. In *ECCV*. Springer, 2022. 2
- [11] Dale Decatur, Itai Lang, and Rana Hanocka. 3D Highlighter: Localizing Regions on 3D Shapes via Text Descriptions. In *CVPR*, 2023. 5, 6
- [12] Boyang Deng, Kyle Genova, Soroosh Yazdani, Sofien Bouaziz, Geoffrey Hinton, and Andrea Tagliasacchi. Cvxnet: Learnable convex decomposition. In *CVPR*, 2020. 2
- [13] Alexey Dosovitskiy, Lucas Beyer, Alexander Kolesnikov, Dirk Weissenborn, Xiaohua Zhai, Thomas Unterthiner, Mostafa Dehghani, Matthias Minderer, Georg Heigold, Sylvain Gelly, Jakob Uszkoreit, and Neil Houlsby. An image is worth 16x16 words: Transformers for image recognition at scale, 2021. 3, 8
- [14] Jensen Gao, Bidipta Sarkar, Fei Xia, Ted Xiao, Jiajun Wu, Brian Ichter, Anirudha Majumdar, and Dorsa Sadigh. Physically grounded vision-language models for robotic manipulation, 2023. 1
- [15] Kyle Genova, Forrester Cole, Avneesh Sud, Aaron Sarna, and Thomas Funkhouser. Local deep implicit functions for 3d shape. In *CVPR*, 2020. 2
- [16] Ankit Goyal, Hei Law, Bowei Liu, Alejandro Newell, and Jia Deng. Revisiting Point Cloud Shape Classification with a Simple and Effective Baseline. *ICML*, 2021. 8
- [17] Meng-Hao Guo, Jun-Xiong Cai, Zheng-Ning Liu, Tai-Jiang Mu, Ralph R. Martin, and Shi-Min Hu. Pct: Point cloud transformer. *Computational Visual Media*, 7(2):187–199, Apr. 2021. 2
- [18] Tong He, Dong Gong, Zhi Tian, and Chunhua Shen. Learning and memorizing representative prototypes for 3d point cloud semantic and instance segmentation. In *ECCV*. Springer, 2020. 2
- [19] Li Jiang, Hengshuang Zhao, Shaoshuai Shi, Shu Liu, Chi-Wing Fu, and Jiaya Jia. Pointgroup: Dual-set point grouping for 3d instance segmentation. In *CVPR*, 2020. 2
- [20] Hyunjin Kim and Minhyuk Sung. Partstad: 2d-to-3d part segmentation task adaptation, 2024. 3
- [21] Alexander Kirillov, Eric Mintun, Nikhila Ravi, Hanzi Mao, Chloe Rolland, Laura Gustafson, Tete Xiao, Spencer Whitehead, Alexander C. Berg, Wan-Yen Lo, Piotr Dollar, and Ross Girshick. Segment anything. In *Proceedings of the IEEE/CVF International Conference on Computer Vision (ICCV)*, pages 4015–4026, October 2023. 2
- [22] Juil Koo, Ian Huang, Panos Achlioptas, Leonidas J Guibas, and Minhyuk Sung. Partglot: Learning shape part segmentation from language reference games. In *CVPR*, 2022. 2
- [23] Junnan Li, Dongxu Li, Silvio Savarese, and Steven Hoi. Blip-2: bootstrapping language-image pre-training with frozen image encoders and large language models. In *Proceedings of the 40th International Conference on Machine Learning, ICML’23*. JMLR.org, 2023. 1
- [24] Liunian Harold Li, Pengchuan Zhang, Haotian Zhang, Jianwei Yang, Chunyuan Li, Yiwu Zhong, Lijuan Wang, Lu Yuan, Lei Zhang, Jenq-Neng Hwang, et al. Grounded language-image pre-training. In *CVPR*, 2022. 1, 2
- [25] Yangyan Li, Rui Bu, Mingchao Sun, Wei Wu, Xinhan Di, and Baoquan Chen. Pointcnn: Convolution on x-transformed points. In S. Bengio, H. Wallach, H. Larochelle, K. Grauman, N. Cesa-Bianchi, and R. Garnett, editors, *NeurIPS*, volume 31. Curran Associates, Inc., 2018. 2
- [26] Victor Weixin Liang, Yuhui Zhang, Yongchan Kwon, Serena Yeung, and James Y Zou. Mind the gap: Understanding the modality gap in multi-modal contrastive representation learning. In S. Koyejo, S. Mohamed, A. Agarwal, D. Belgrave, K. Cho, and A. Oh, editors, *NeurIPS*. Curran Associates, Inc., 2022. 1

- [27] Jinxian Liu, Minghui Yu, Bingbing Ni, and Ye Chen. Self-prediction for joint instance and semantic segmentation of point clouds. In *ECCV*. Springer, 2020. 2
- [28] Minghua Liu, Yinhao Zhu, Hong Cai, Shizhong Han, Zhan Ling, Fatih Porikli, and Hao Su. Partslip: Low-shot part segmentation for 3d point clouds via pretrained image-language models. In *CVPR*, 2023. 1, 2, 3, 5, 6
- [29] Jonathan Masci, Davide Boscaini, Michael Bronstein, and Pierre Vandergheynst. Geodesic convolutional neural networks on riemannian manifolds. In *ICCV*, 2015. 2
- [30] Kaichun Mo, Shilin Zhu, Angel X. Chang, Li Yi, Subarna Tripathi, Leonidas J. Guibas, and Hao Su. PartNet: A large-scale benchmark for fine-grained and hierarchical part-level 3D object understanding. In *CVPR*, June 2019. 2, 5, 6
- [31] Xin Ning, Zaiyang Yu, Lusi Li, Weijun Li, and Prayag Tiwari. Dirlf: Differentiable rendering-based multi-view image-language fusion for zero-shot 3d shape understanding. *Information Fusion*, 102:102033, 2024. 2
- [32] Chengjie Niu, Manyi Li, Kai Xu, and Hao Zhang. Rimnet: Recursive implicit fields for unsupervised learning of hierarchical shape structures. In *CVPR*, 2022. 2
- [33] Maxime Oquab, Timothée Darcet, Théo Moutakanni, Huy Vo, Marc Szafraniec, Vasil Khalidov, Pierre Fernandez, Daniel Haziza, Francisco Massa, Alaaeldin El-Nouby, et al. DINOv2: Learning robust visual features without supervision. *arXiv preprint arXiv:2304.07193*, 2023. 1, 2, 3, 5, 8
- [34] Despoina Paschalidou, Angelos Katharopoulos, Andreas Geiger, and Sanja Fidler. Neural parts: Learning expressive 3d shape abstractions with invertible neural networks. In *CVPR*, 2021. 2
- [35] Despoina Paschalidou, Ali Osman Ulusoy, and Andreas Geiger. Superquadrics revisited: Learning 3d shape parsing beyond cuboids. In *CVPR*, 2019. 2
- [36] Charles R Qi, Hao Su, Kaichun Mo, and Leonidas J Guibas. Pointnet: Deep learning on point sets for 3d classification and segmentation. In *CVPR*, 2017. 2
- [37] Charles Ruizhongtai Qi, Li Yi, Hao Su, and Leonidas J Guibas. Pointnet++: Deep hierarchical feature learning on point sets in a metric space. *NeurIPS*, 2017. 2
- [38] Zheyun Qin, Cheng Han, Qifan Wang, Xiushan Nie, Yilong Yin, and Lu Xiankai. Unified 3d segmenter as prototypical classifiers. *NeurIPS*, 2023. 2
- [39] Alec Radford, Jong Wook Kim, Chris Hallacy, Aditya Ramesh, Gabriel Goh, Sandhini Agarwal, Girish Sastry, Amanda Askell, Pamela Mishkin, Jack Clark, Gretchen Krueger, and Ilya Sutskever. Learning transferable visual models from natural language supervision. In Marina Meila and Tong Zhang, editors, *Proceedings of the 38th International Conference on Machine Learning*, volume 139 of *Proceedings of Machine Learning Research*, pages 8748–8763. PMLR, 18–24 Jul 2021. 1, 2, 5, 8
- [40] Martin Simonovsky and Nikos Komodakis. Dynamic edge-conditioned filters in convolutional neural networks on graphs. In *CVPR*, 2017. 2
- [41] Hugues Thomas, Charles R Qi, Jean-Emmanuel Deschaud, Beatriz Marcotequi, François Goulette, and Leonidas J Guibas. Kpconv: Flexible and deformable convolution for point clouds. In *ICCV*, 2019. 2
- [42] Shubham Tulsiani, Hao Su, Leonidas J Guibas, Alexei A Efros, and Jitendra Malik. Learning shape abstractions by assembling volumetric primitives. In *CVPR*, 2017. 2
- [43] Vishaal Udandarao, Ankush Gupta, and Samuel Albanie. Susx: Training-free name-only transfer of vision-language models. In *ICCV*, 2023. 1
- [44] Ardian Umam, Cheng-Kun Yang, Min-Hung Chen, Jen-Hui Chuang, and Yen-Yu Lin. Partdistill: 3d shape part segmentation by vision-language model distillation, 2023. 2
- [45] Mikaela Angelina Uy, Quang-Hieu Pham, Binh-Son Hua, Duc Thanh Nguyen, and Sai-Kit Yeung. Revisiting point cloud classification: A new benchmark dataset and classification model on real-world data. In *ICCV*, 2019. 2, 3, 5, 6, 7
- [46] Petar Veličković, Guillem Cucurull, Arantxa Casanova, Adriana Romero, Pietro Liò, and Yoshua Bengio. Graph attention networks, 2018. 2
- [47] Thang Vu, Kookhoi Kim, Tung M Luu, Thanh Nguyen, and Chang D Yoo. Softgroup for 3d instance segmentation on point clouds. In *CVPR*, pages 2708–2717, 2022. 2
- [48] Ruocheng Wang, Yunzhi Zhang, Jiayuan Mao, Ran Zhang, Chin-Yi Cheng, and Jiajun Wu. Ikea-manual: Seeing shape assembly step by step. *NeurIPS*, 2022. 2
- [49] Weiye Wang, Ronald Yu, Qiangui Huang, and Ulrich Neumann. Sgpn: Similarity group proposal network for 3d point cloud instance segmentation. In *CVPR*, 2018. 2
- [50] Yuheng Xue, Nenglu Chen, Jun Liu, and Wenyun Sun. Ze-rops: High-quality cross-modal knowledge transfer for zero-shot 3d part segmentation, 2023. 1, 2, 5, 6
- [51] Cheng-Kun Yang, Yung-Yu Chuang, and Yen-Yu Lin. Unsupervised point cloud object co-segmentation by co-contrastive learning and mutual attention sampling. In *ICCV*, 2021. 2
- [52] Li Yi, Vladimir G Kim, Duygu Ceylan, I-Chao Shen, Mengyan Yan, Hao Su, Cewu Lu, Qixing Huang, Alla Sheffer, and Leonidas Guibas. A scalable active framework for region annotation in 3d shape collections. *ACM Transactions on Graphics*, 35(6):1–12, 2016. 2, 5, 6, 7
- [53] Li Yi, Wang Zhao, He Wang, Minhyuk Sung, and Leonidas J Guibas. Gspn: Generative shape proposal network for 3d instance segmentation in point cloud. In *CVPR*, 2019. 2
- [54] Biao Zhang and Peter Wonka. Point cloud instance segmentation using probabilistic embeddings. In *CVPR*, 2021. 2
- [55] Renrui Zhang, Ziyu Guo, Wei Zhang, Kunchang Li, Xupeng Miao, Bin Cui, Yu Qiao, Peng Gao, and Hongsheng Li. Point-clip: Point cloud understanding by clip. In *CVPR*, 2022. 1, 2, 3, 5, 6
- [56] Yangheng Zhao, Jun Wang, Xiaolong Li, Yue Hu, Ce Zhang, Yanfeng Wang, and Siheng Chen. Number-adaptive prototype learning for 3d point cloud semantic segmentation. In *ECCV*. Springer, 2022. 2
- [57] Yuchen Zhou, Jiayuan Gu, Xuanlin Li, Minghua Liu, Yinhao Fang, and Hao Su. Partslip++: Enhancing low-shot 3d part segmentation via multi-view instance segmentation and maximum likelihood estimation, 2023. 1, 2, 3, 6
- [58] Chenyang Zhu, Kai Xu, Siddhartha Chaudhuri, Li Yi, Leonidas J Guibas, and Hao Zhang. Adacoseg: Adaptive shape co-segmentation with group consistency loss. In *CVPR*, 2020. 2



- [59] Xiangyang Zhu, Renrui Zhang, Bowei He, Ziyu Guo, Ziyao Zeng, Zipeng Qin, Shanghang Zhang, and Peng Gao. Point-clip v2: Prompting clip and gpt for powerful 3d open-world learning. In *ICCV*, 2023. [1](#), [2](#), [3](#), [5](#), [6](#), [7](#), [8](#)

# Supplementary material for 3D Part Segmentation via Geometric Aggregation of 2D Visual Features

Marco Garosi

University of Trento

marco.garosi@unitn.it

Massimiliano Mancini

University of Trento

massimiliano.mancini@unitn.it

Riccardo Tedoldi

University of Trento

riccardo.tedoldi@unitn.it

Nicu Sebe

University of Trento

sebe@disi.unitn.it

Davide Boscaini

Fondazione Bruno Kessler

dboscaini@fbk.eu

Fabio Poiesi

Fondazione Bruno Kessler

poiesi@fbk.eu

## A. Introduction

We provide additional material in support of our main paper. This document is organised as follows:

- In Appendix B, we describe the steps involved in COPS and we show them qualitatively on some point clouds.
- In Appendix C, we provide implementation details of COPS and specify the hyper-parameter used in our experiments to facilitate reproducibility.
- In Appendix D, we ablate the role of the specific layer of the DINOv2-Base architecture from which we perform feature extraction.
- In Appendix E, we investigate the role of the number of spatial and semantic nearest neighbours used in the Geometric Feature Aggregation (GFA) module.
- In Appendix F, we provide additional qualitative results on ScanObjectNN [9] and FAUST [2] datasets.
- In Appendix G, we provide details on the computational resources utilised.

## B. Pipeline visualisation

In Fig. 1, we provide a detailed visualisation of the different steps required by COPS on four point clouds from ShapeNetPart [11]. The first three columns illustrate the feature extractor  $\Phi$ , which processes the input point cloud depicted in the first column, extracts features using DINOv2 [6] (second column), and modifies them using the Geometric Feature Aggregation (GFA) module (third column). The next three columns illustrate the segmenter  $\Psi$ , which decomposes the object into parts via feature clustering (fourth column, colours are not informative) and assigns each part a semantic label (sixth column) by leveraging PointCLIPv2 [12] predictions (fifth column) as semantic anchors. The last column displays the ground-truth segmentation. The minimal difference between the last two columns suggests that COPS produces very accurate segmentations, despite the low

quality of the PointCLIPv2 predictions shown in the fifth column.

## C. Implementation details

In this section, we discuss implementation details and the hyper-parameters of COPS.

**Point cloud processing.** We perform rendering at the original point cloud resolution to retain finer details. Then, we randomly sample 10,000 points from each object, we update the pixel-to-point mappings utilised to back-project features to 3D, and we project them back. Next, GFA performs farthest point sampling (FPS) to find super points for feature aggregation. Subsequently, we randomly sample 2,048 points to obtain semantic labels via PointCLIPv2. Lastly, we perform clustering on these sampled points and we assign each cluster a semantic label via Hungarian with PointCLIPv2’s predictions.

**Rendering.** We utilise PyTorch3D [8] for rendering. Notably, we set: (i) camera orientations, (ii) point size, and (iii) rendering canvas size. We have defined three camera settings: 6 orthogonal cameras, facing front, back, left, right, top, and bottom in Fig. 2(a); 10 cameras, following PointCLIPv2 [12] in Fig. 2(b); 48 cameras in Fig. 2(c). We set the point size to small values for datasets whose point clouds are *dense*, i.e., containing many points. We enlarge the point size for *sparse* datasets, such as ShapeNetPart, to obtain smooth renders. Lastly, we set the canvas size to the input size of DINOv2 of  $224 \times 224$  pixels, ensuring no scaling and/or cropping is required. When photometric (RGB) information is not available, we render depth maps. We utilise both the depth maps produced by PyTorch3D, where light pixels correspond to close points, and the depth maps in PointCLIPv2’s style, where the dark pixels correspond to points close to the camera. We found COPS to perform the best with PyTorch3D’s depth maps.

**Feature extraction.** DINOv2 is based on the vision trans-

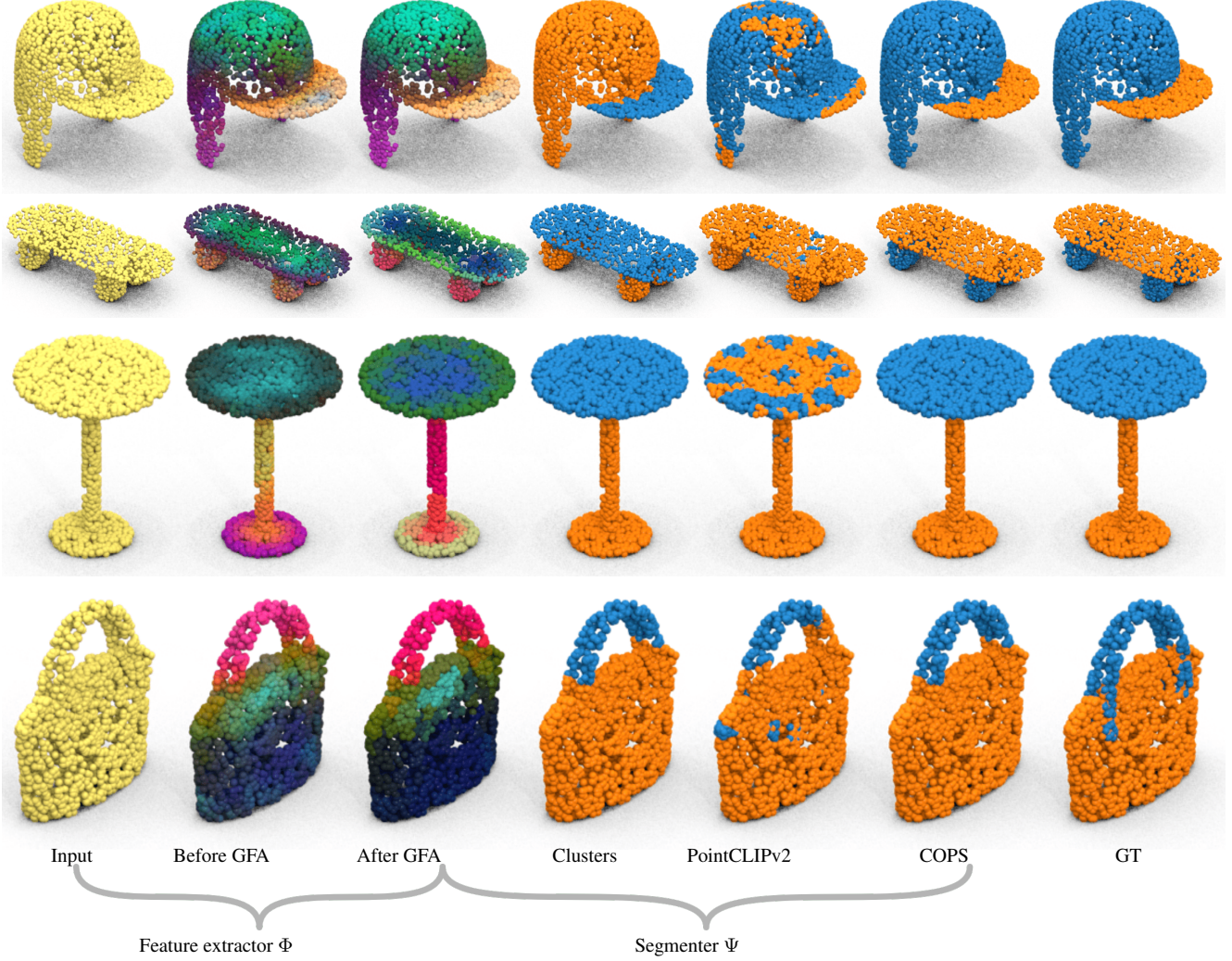


Figure 1. Detailed visualisation of the steps required by COPS. From left to right: input point cloud, intermediate features obtained by 3D-lifting DINOv2 features, final features obtained with GFA, part decomposition obtained via feature clustering (colours are not informative because cluster labels are not semantic), PointCLIPv2 predictions, COPS predictions, and ground-truth segmentation. By disentangling part decomposition (fourth column) from semantic label assignment, COPS can leverage noisy PointCLIPv2 predictions (fifth column) to produce accurate segmentations (sixth column).

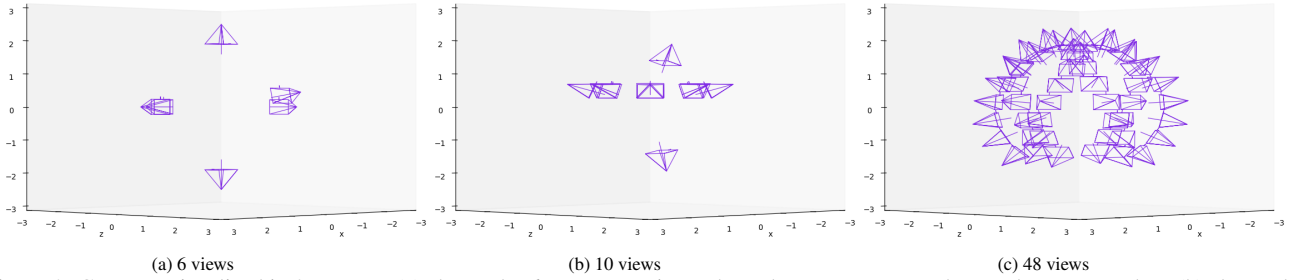


Figure 2. Cameras visualised in 3D space. (a) shows the 6-camera setting, where the cameras are orthogonal to one another. (b) shows the 10 cameras adapted from PointCLIPv2 [12]. They capture the object from more sides, while the top and bottom views are similar to those in (a). (c) shows the largest setting, with 48 cameras sampled bottom to top on eight arches around the object. While this configuration provides more views than (a) and (b), there are many redundant views which contribute little to the overall performance, as we have shown in the corresponding ablation study.



former architecture [3, 10]. It splits the image into patches of  $14 \times 14$  pixels and outputs a feature vector for each patch. However, we need pixel-level, or dense, features to perform lifting to 3D. Therefore, we upsample the feature maps to the input image size of  $224 \times 224$  pixels using bicubic interpolation.

**Geometric feature aggregation (GFA).** GFA works in three steps: (i) it samples super points, (ii) it aggregates features via either spatial or semantic attention, and (iii) it upsamples super point features to the whole point cloud. GFA has two hyper-parameters: the number of super points and the number of neighbours considered in the aggregation step. For the first, too many super points may lead to reduced spatial/semantic consistency, while too few can make the features collapse, not accounting for the local variability of the point cloud. By default, we sample 256 super points. For the second, the more the points and the larger the context window used to compute the super point’s feature. By default, we set it to 10 for spatial attention and to 90 for semantic attention. In Appendix E, we conduct an ablation study on these hyper-parameters.

## D. Ablation study on DINOv2-Base layers

Following FoundPose [7], in Tab. 1 we evaluate COPS with different patch descriptors. We utilise DINOv2-Base (ViT-B) and sample patch-level features at different levels, showing how performance changes. We observe an increment in performance as we utilise increasingly higher-level patch descriptors, which encode more abstract semantic information, *e.g.*, about parts [6]. We note that performance improves in certain categories, such as “airplane”, as we move towards higher-level representations. However, we find that for other categories, such as “mug” or “knife”, lower-level representations may provide the optimal level of abstraction for achieving accurate part segmentation results. This highlights the need for further exploration in future work, assessing how to consider representations at different scales to achieve consistent improvements.

## E. Ablation study on GFA

In Tab. 2(a), we conduct an additional ablation study on the GFA module. We evaluate 13 distinct configurations, including the standard GFA employed in the main paper. Specifically, we vary the number of sampled super points, the number of neighbours taken into account during the attention operation, *i.e.*, the “context window”, and weighting by distance. In Tab. 2(b) we repeat these experiments by swapping the order of spatially- and semantically-consistent feature aggregation. The results show that our default configuration performs the best. We observe that increasing the number of neighbours reduces performance, thus suggesting that a smaller “context window” allows GFA to aggregate

only the most relevant features. Raising the number of super points leads to a decrease in performance because it limits the effect of GFA. If all the points are kept as super points, GFA has no effect, while if too few super points are sampled, features can collapse. Lastly, performing spatially-before semantically-consistent feature aggregation makes GFA capture geometric knowledge better, thus achieving higher performance.

## F. Additional qualitative results

Following our main paper, we show additional qualitative results on other datasets. Fig. 4 shows qualitative results on FAUST [2], using annotations from SATR [1]. Fig. 3 shows qualitative results on ScanObjectNN [9] in the most challenging OBJ-BG setting. Objects such as “bed” or “sofa” pose challenges in distinguishing between the individual parts due to overlapping geometry or intricate designs. Moreover, the real-world point clouds in ScanObjectNN [9] are noisy and can contain several occlusions, making it difficult to separate them into distinct parts.

## G. Resources used

Our training-free method does not require extensive computational resources and is designed to be computationally efficient. We run all our experiments on a consumer desktop NVIDIA RTX 3060 GPU with 12GB of VRAM and a laptop NVIDIA RTX 2070 Super Max-q with 8GB of VRAM. Evaluation time on the NVIDIA RTX 3060 GPU took approximately: 40 seconds on FAUST [1]; 1 hour on ScanObjectNN [9]; 3 hours on PartNetE [4]; 9 hours on ShapeNetPart [11]; 12 hours on PartNet [5]. All the reported inference times are doubled if running the inference on the consumer laptop with the NVIDIA RTX 2070 GPU with 8GB of VRAM. Further optimisations, such as pre-rendering views for all objects, can be introduced to lower test times. However, they can take up a large amount of storage space.

## References

- [1] Ahmed Abdelreheem, Ivan Skorokhodov, Maks Ovsjanikov, and Peter Wonka. SATR: Zero-Shot Semantic Segmentation of 3D Shapes. In *ICCV*, 2023. 3, 6
- [2] Federica Bogo, Javier Romero, Matthew Loper, and Michael J. Black. FAUST: Dataset and evaluation for 3D mesh registration. In *CVPR*, 2014. 1, 3, 6
- [3] Alexey Dosovitskiy, Lucas Beyer, Alexander Kolesnikov, Dirk Weissenborn, Xiaohua Zhai, Thomas Unterthiner, Mostafa Dehghani, Matthias Minderer, Georg Heigold, Sylvain Gelly, Jakob Uszkoreit, and Neil Houlsby. An image is worth 16x16 words: Transformers for image recognition at scale, 2021. 3
- [4] Minghua Liu, Yinhao Zhu, Hong Cai, Shizhong Han, Zhan Ling, Fatih Porikli, and Hao Su. Partslip: Low-shot part seg-

ViT-B layer	mIoU <sub>l</sub>	mIoU <sub>c</sub>	Airplane	Bag	Cap	Car	Chair	Earphone	Guitar	Knife	Lamp	Laptop	Motorbike	Mug	Pistol	Rocket	Skate	Table
1 0	49.7	46.4	31.1	53.0	45.7	27.9	47.5	50.8	60.7	66.6	45.5	71.3	21.6	42.9	35.6	31.0	48.8	61.8
2 1	55.9	52.1	31.5	72.9	65.2	29.9	60.6	56.0	47.7	62.9	45.9	90.0	22.6	58.4	39.8	29.5	50.0	70.3
3 2	58.4	51.6	32.3	65.2	49.2	32.2	66.0	55.7	50.9	68.9	46.8	90.6	23.9	43.9	42.7	31.4	52.5	72.7
4 3	58.8	52.5	33.1	64.4	54.5	32.9	66.4	55.3	48.7	72.6	47.2	92.0	23.7	53.4	40.1	31.2	52.1	72.7
5 6	60.5	55.2	36.8	53.8	65.4	32.2	68.0	60.8	66.6	78.5	48.4	91.1	24.6	36.5	48.9	45.7	53.3	71.8
6 7	61.0	56.4	41.1	59.9	64.4	31.8	68.2	63.5	67.2	80.1	48.4	88.9	24.8	41.1	49.6	47.0	55.6	71.0
7 8	61.4	56.3	43.2	60.7	61.6	31.8	68.4	64.7	67.1	77.5	48.2	90.1	25.1	40.3	49.8	45.8	55.1	71.7
8 10	62.6	59.0	50.7	64.7	71.1	30.5	69.0	66.2	70.2	81.6	48.7	77.9	25.3	60.1	52.2	47.6	56.3	71.2
9 11	63.3	60.1	50.6	70.7	69.8	29.7	70.0	66.0	66.2	79.7	49.0	86.8	25.9	68.2	53.5	46.0	57.5	72.1
10 12 (w/o norm.)	64.0	61.1	50.9	75.8	69.5	29.7	71.2	66.4	68.8	76.5	48.8	89.2	25.1	72.4	56.4	47.6	56.8	72.8
11 12 (w/ norm.)	64.4	60.9	51.3	71.0	69.7	29.9	71.7	66.4	72.6	80.2	48.6	91.1	26.1	62.5	54.3	46.7	59.4	72.9

Table 1. Part segmentation performance on ShapeNetPart [11] obtained when extracting DINOv2 base features from different layers, *i.e.*, at different depths. DINOv2 base is based on ViT-B, and has 13 layers. The highlighted row corresponds to the results shown in the main paper.

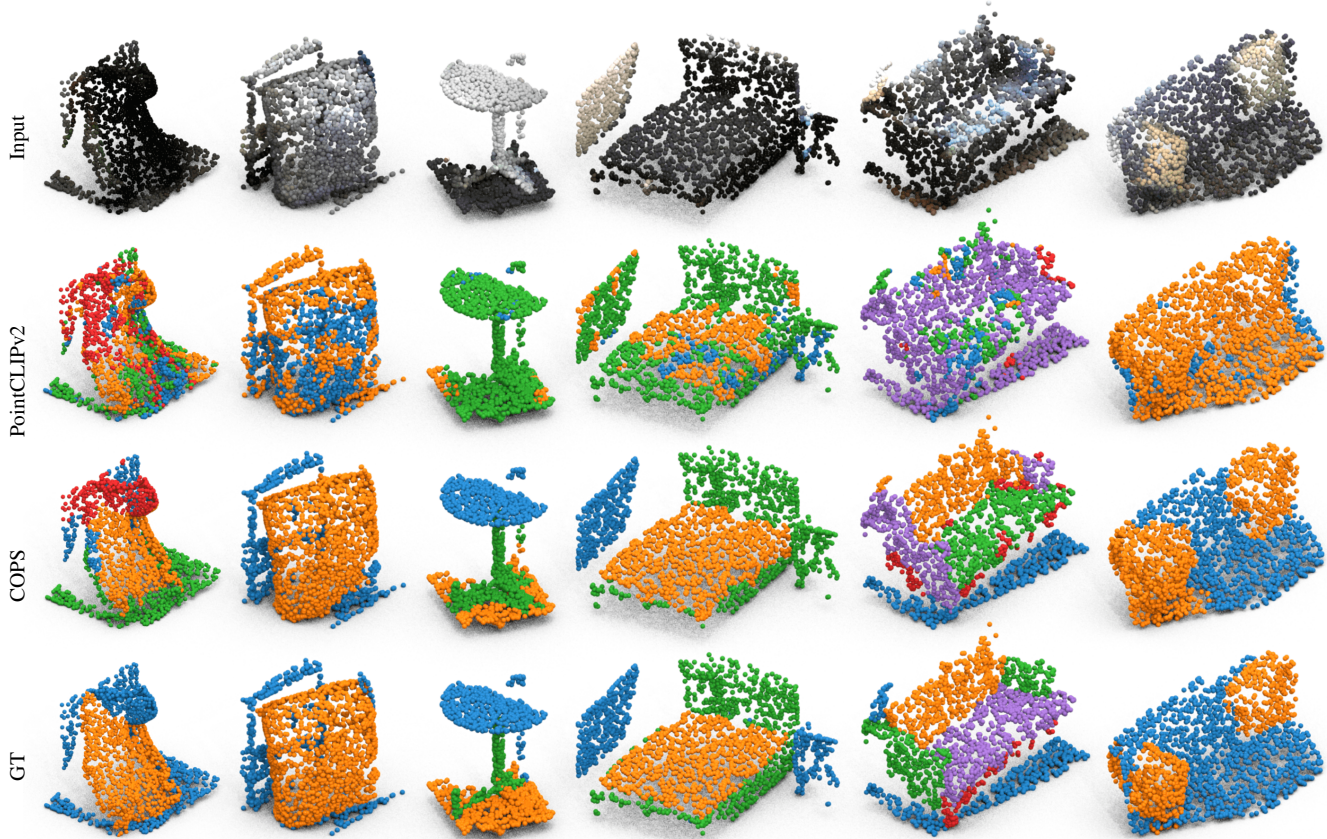


Figure 3. Qualitative results on ScanObjectNN [9]. Top to bottom: input point cloud with RGB colours, PointCLIPv2 predictions, COPS predictions, and ground-truth segmentation.

mentation for 3d point clouds via pretrained image-language models. In *CVPR*, 2023. 3

scale benchmark for fine-grained and hierarchical part-level 3D object understanding. In *CVPR*, June 2019. 3

[5] Kaichun Mo, Shilin Zhu, Angel X. Chang, Li Yi, Subarna Tripathi, Leonidas J. Guibas, and Hao Su. PartNet: A large-

[6] Maxime Oquab, Timothée Darcet, Théo Moutakanni, Huy Vo, Marc Szafraniec, Vasil Khalidov, Pierre Fernandez, Daniel

		Sup. spat.	Sup. sem.	Nei. spat.	Nei. sem.	mIoU <sub>I</sub>	mIoU <sub>C</sub>	Airplane	Bag	Cap	Car	Chair	Earphone	Guitar	Knife	Lamp	Laptop	Motorbike	Mug	Pistol	Rocket	Skate	Table
Superpoints	1	512	256	10	90	64.2	60.0	50.6	68.3	69.2	30.1	71.6	65.4	74.2	78.6	48.9	90.9	26.3	58.1	52.9	45.5	57.3	72.7
	2	256	512			64.3	60.7	51.0	70.6	70.0	29.7	71.5	64.8	72.0	79.0	48.9	91.6	26.1	63.3	53.8	46.4	59.5	73.0
	3	512	512			64.3	60.8	50.9	71.4	70.1	29.7	71.2	65.8	73.7	78.6	48.5	91.2	26.2	62.9	52.3	48.0	59.6	73.1
	4	128	256			64.3	61.0	51.0	68.9	72.1	30.0	71.7	66.0	70.5	79.0	48.9	91.4	25.5	64.3	55.9	49.0	59.4	72.8
	5	256	128			64.2	60.3	51.4	66.0	72.0	29.9	71.7	65.2	70.9	78.9	48.9	91.0	25.8	62.9	53.1	48.1	57.2	72.6
	6	128	128			64.3	60.5	50.7	73.3	67.0	29.6	71.5	66.5	72.1	80.3	49.1	91.0	25.8	55.7	56.2	47.7	59.4	73.0
Neighbours	7			10	90	64.4	60.9	51.3	71.0	69.7	29.9	71.7	66.4	72.6	80.2	48.6	91.1	26.1	62.5	54.3	46.7	59.4	72.9
	8			90	90	61.9	58.6	49.6	62.8	68.9	28.0	67.8	64.0	73.3	80.3	48.5	89.0	24.9	58.9	54.9	42.1	55.0	69.5
	9	256	256	170	256	58.6	54.9	49.0	59.5	69.3	25.3	62.8	60.4	70.5	79.5	48.3	86.6	23.9	32.1	53.5	46.4	46.3	65.6
	10			90	10	61.2	58.5	49.1	68.0	66.7	27.3	68.2	64.7	69.6	79.3	48.4	90.7	24.6	54.5	53.8	46.5	55.0	69.2

(a) Spatially-consistent aggregation followed by semantically-consistent aggregation

		Sup. sem.	Sup. spat.	Nei. sem.	Nei. spat.	mIoU <sub>I</sub>	mIoU <sub>C</sub>	Airplane	Bag	Cap	Car	Chair	Earphone	Guitar	Knife	Lamp	Laptop	Motorbike	Mug	Pistol	Rocket	Skate	Table
Superpoints	1	256	512	90	10	63.9	60.3	50.6	74.1	68.3	29.2	71.3	65.5	71.4	78.4	48.5	90.9	26.3	61.0	51.2	46.4	58.9	72.6
	2	512	256			64.2	60.3	50.8	70.5	68.2	29.9	71.1	65.6	74.1	80.1	48.7	91.3	26.4	54.9	53.6	48.6	58.6	72.9
	3	512	512			63.9	60.1	50.2	71.5	71.0	29.2	71.0	65.6	72.0	79.2	48.6	91.0	26.4	55.1	53.7	46.7	57.9	73.0
	4	256	128			64.2	60.4	50.6	69.7	66.7	30.1	71.6	65.5	72.5	80.4	48.6	91.1	25.8	63.3	54.9	46.4	56.1	72.6
	5	128	256			64.1	60.3	50.7	71.4	68.1	29.6	71.3	65.3	72.1	79.7	48.6	91.0	26.2	59.3	53.9	46.7	58.6	72.7
	6	128	128			64.0	59.9	50.2	67.5	65.8	29.6	71.7	65.2	71.8	80.4	48.9	90.8	26.8	60.1	53.5	44.7	58.7	72.5
Neighbours	7			90	10	64.1	60.4	50.7	64.7	68.2	30.0	71.4	65.2	72.2	79.2	48.4	91.1	26.0	67.0	54.0	47.8	58.3	72.7
	8			90	90	61.8	58.8	49.3	69.7	69.2	27.4	67.9	63.9	74.4	79.7	48.5	89.9	25.0	52.6	52.2	47.9	53.7	69.4
	9	256	256	256	170	59.0	55.3	47.6	59.8	67.3	25.1	64.8	60.9	69.2	80.3	48.2	89.2	24.0	36.5	51.4	46.7	48.8	65.7
	10			10	90	61.6	58.1	49.3	66.4	66.9	27.1	68.3	64.1	72.1	79.7	48.3	90.5	26.3	46.5	53.1	48.7	54.2	68.9

(b) Semantically-consistent aggregation followed by spatially-consistent aggregation

Table 2. Ablation on the geometric feature extractor (GFA) module on ShapeNetPart [11]. Results were obtained using 10 rendered (depth only) views. All experiments use a two-stage GFA. Panels (a) and (b) show how performance changes when swapping the two stages. Each of the first two groups of columns reports the configuration for the two stages. “Sup.” is the number of super points sampled from the input point cloud. “Nei.” is the number of neighbours considered during the aggregation phase. The highlighted row corresponds to the results shown in the main paper.

- Haziza, Francisco Massa, Alaaeldin El-Nouby, et al. DINOv2: Learning robust visual features without supervision. *arXiv preprint arXiv:2304.07193*, 2023. 1, 3
- [7] Evin Pinar Örneke, Yann Labbé, Bugra Tekin, Lingni Ma, Cem Keskin, Christian Forster, and Tomas Hodan. Foundpose: Unseen object pose estimation with foundation features. *arXiv preprint arXiv:2311.18809*, 2023. 3
- [8] Nikhila Ravi, Jeremy Reizenstein, David Novotny, Taylor Gordon, Wan-Yen Lo, Justin Johnson, and Georgia Gkioxari. Accelerating 3d deep learning with pytorch3d. *arXiv:2007.08501*, 2020. 1
- [9] Mikaela Angelina Uy, Quang-Hieu Pham, Binh-Son Hua, Duc Thanh Nguyen, and Sai-Kit Yeung. Revisiting point cloud classification: A new benchmark dataset and classification model on real-world data. In *ICCV*, 2019. 1, 3, 4
- [10] Ashish Vaswani, Noam Shazeer, Niki Parmar, Jakob Uszkoreit, Llion Jones, Aidan N Gomez, Łukasz Kaiser, and Illia Polosukhin. Attention is all you need. *NeurIPS*, 2017. 3
- [11] Li Yi, Vladimir G Kim, Duygu Ceylan, I-Chao Shen, Mengyan Yan, Hao Su, Cewu Lu, Qixing Huang, Alla Sheffer, and Leonidas Guibas. A scalable active framework for region annotation in 3d shape collections. *ACM Transactions on Graphics*, 35(6):1–12, 2016. 1, 3, 4, 5
- [12] Xiangyang Zhu, Renrui Zhang, Bowei He, Ziyu Guo, Ziyao Zeng, Zipeng Qin, Shanghang Zhang, and Peng Gao. Point-clip v2: Prompting clip and gpt for powerful 3d open-world learning. In *ICCV*, 2023. 1, 2



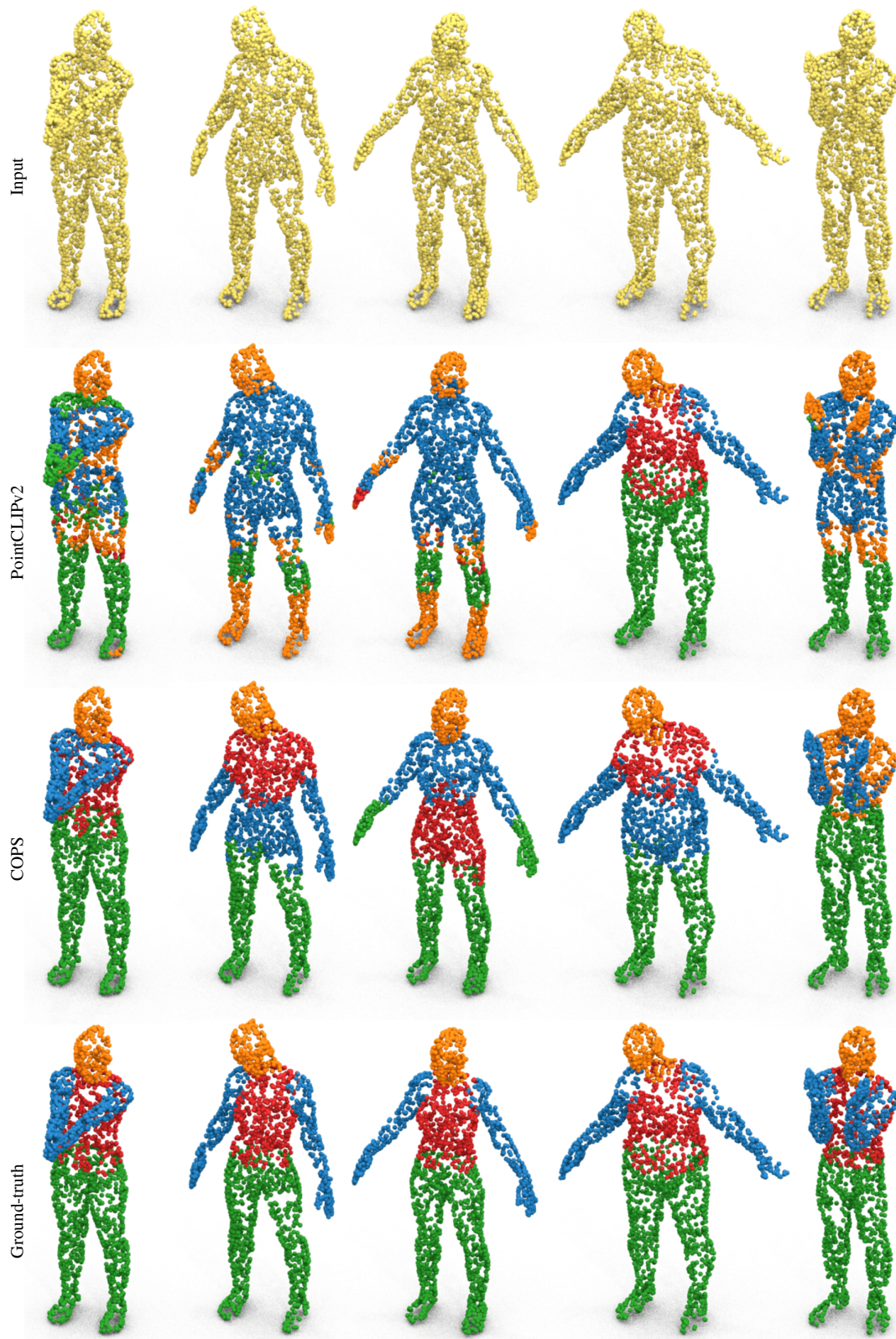


Figure 4. Qualitative results on FAUST [2]. Top to bottom: input texture-less point cloud (coloured in yellow for visualisation purposes), PointCLIPv2 predictions, COPS predictions, and ground-truth segmentation provided by SATR [1].